Nonlinear material and ionic transport through membrane nanotubes

D.V. Ivchenkov [a,b], P.I. Kuzmin [c], T.R. Galimzyanov [c], A.V. Shnyrova [d,e], P.V. Bashkirov [a,b,*], V. A. Frolov [d,e,f,**]

[a] Federal Research and Clinical Center of Physical-Chemical Medicine, Moscow 119435, Russia
[b] Department of Molecular and Biological Physics, Moscow Institute of Physics and Technology, Institutskiy lane 9, Dolgoprudnyy, Moscow region 141700, Russia
[c] A.N. Frumkin Institute of Physical Chemistry and Electrochemistry, Russian Academy of Sciences, Moscow 119071, Russia
[d] Biofisika Institute (CSIC, UPV/EHU), University of the Basque Country, barrio Sarriena s/n, 48940 Leioa, Spain
[e] Department of Biochemistry and Molecular Biology, University of the Basque Country, barrio Sarriena s/n, 48940 Leioa, Spain
[f] Ikerbasque, Basque Foundation for Science, Maria Diaz de Haro 3, 6 solairua, 48013 Bilbao, Spain

ARTICLE INFO

ABSTRACT

Membrane nanotubes (NTs) and their networks play an important role in intracellular membrane transport and intercellular communications. The transport characteristics of the NT lumen resemble those of conventional solid-state nanopores. However, unlike the rigid pores, the soft membrane wall of the NT can be deformed by forces driving the transport through the NT lumen. This intrinsic coupling between the NT geometry and transport properties remains poorly explored. Using synchronized fluorescence microscopy and conductance measurements, we revealed that the NT shape was changed by both electric and hydrostatic forces driving the ionic and solute fluxes through the NT lumen. Far from the shape instability, the strength of the force effect is determined by the lateral membrane tension and is scaled with membrane elasticity so that the NT can be operated as a linear elastic sensor. Near shape instabilities, the transport forces triggered large-scale shape transformations, both stochastic and periodic. The periodic oscillations were coupled to a vesicle passage along the NT axis, resembling peristaltic transport. The oscillations were parametrically controlled by the electric field, making NT a highly nonlinear nanofluidic circuitry element with biological and technological implications.

1. Introduction

Membrane nanotubes (NTs) are one of the core elements of the endomembrane system. Dynamic nanotubular networks, such as tubular endoplasmic reticulum, mediate the long-range communication throughout the cytoplasm [1–3]. Short and transient tubular connections, such as membrane fusion and fission pores, regularly appear in membrane remodeling [4]. An entirely different class of nanotubular connections, the tunneling nanotubes (TNT), is deeply implicated into intercellular transport [5,6]. Complex nanotubular networks could be replicated in vitro, as from cellular [7] as from synthetic components [8,9]. In all of those systems individual NTs operate as a versatile nanofluidic connector transporting solids and fluids through their lumen. The permeability and size selectivity of the NT connectors depend critically on the membrane curvature. Extreme NT constriction severely impairs the luminal transport and could also cause NT scission [10,11]. The high curvature of the wall underlies another function of NT

connectors in the cell. They provide a versatile platform for various protein machineries relying on membrane curvature for self-assembly and function, including those controlling the NT curvature and stability per se [4,11,12]. The mechanisms underlying molecular regulation of the NT curvature, the intrinsic coupling between the curvature and composition, have long been studied using individual NTs produced in biomimetic or cellular membrane systems.

In the cell, individual membrane tubules are frequently produced by molecular motors or filaments creating a pulling force along the parent membrane normal [13,14]. The nanotube puling could be replicated in vitro using either mechanical micromanipulators or optical tweezers [15–17]. The NTs pulled from pure lipid membranes have been widely used for quantitative assessment of visco-elastic properties of lipid bilayer and intricate relations between the molecular composition and curvature of the NT [11,16,18,19]. Decades-long studies revealed a variety of mechanisms controlling the NT curvature and thus the luminal permeability of the NT connectors [19,20]. In the simplest case

of a "reference" single-component lipid reservoir, the static radius of a pulled NT is fully defined by the reservoir membrane's lateral tension and bending rigidity [17,21]. The radius ranges from a few to hundreds of nanometers while its length stretches from below 100 nm to hundreds of microns [16,17,22,23]. Such geometric variability makes the lipid NT a versatile building block for the fabrication of nanoscale transport systems [9,23]. However, the NT and NT networks have been rarely used to study the corresponding transport mechanisms [9,23,24].

The basic principles of material transport through the NT lumen shall be well understood as the NT lumen geometry closely resembles that of a cylindrical solid-state nanopore [25]. The nanopore (NP) surface can even be covered by a lipid layer, thus mimicking the fluidity of the NT wall [26]. Ionic and material transport through the NPs comparable in size with the NTs has been extensively studied. In general, the NPs are nonlinear circuitry elements, with the major transport characteristics controlled by the NP shape, size, and wall coating and charge [26,27]. Some of the wall charge effects, such as the increase of the electrolyte concentration in the pore lumen, have been described in the NT system [17,28]. The NT dimensions, controlled by the molecular composition of the NT membrane and external forces, can be reduced close to molecular dimensions characteristic for NPs capable of molecular sensing [17,29]. Furthermore, the external force can contract or expand the NT lumen in real-time [17]. Such manipulation of nanofluidic transport via elastic coupling to external media has been shown for protein channels and elastic nanopores [30,31]. However, unlike most of the NPs, high bending compliance of the NT membrane makes the NT body susceptible to even small external forces produced by single proteins and protein complexes [17]. The very forces driving the material transport through the NT lumen, including the electrical field [17,32], could deform the NT and thus affect its transport properties. These feedback effects, linking the nanofluidic transport with nanoscale membrane elasticity, are unique for the NT systems and remain poorly explored.

To model these feedback effects, we focus here on the NT deformations produced by transmembrane (TM) electric field. The TM field generally emerges when an electrical potential difference (the bias) is applied between the NT ends to drive the ionic current through the NT lumen [32]. The TM field is known to produce membrane movements along the electrical potential gradient [33,34]. We showed earlier that such an electro-actuation altered the current/voltage characteristic of the NT proportionally to the membrane bending elasticity [17]. Here, we visualized and quantified this effect by applying synchronized fluorescence microscopy and voltage-clamp conductance measurements to microscopic NTs mimicking tunneling nanotubes [22]. We revealed the NT dilation coupled to the ionic transport through the NT lumen. We further revealed that the parabolic expansion of the NT lumen could be described by a single parameter, the effective radius, fully characterizing the nonlinear current/voltage characteristic of the NT. Remarkably, we also found that near shape instability points [35], the TM field could trigger large-scale shape transformation of the nanotube, both stochastic and periodic. While the stochastic oscillations were linked to the catenoid-cylinder shape transformation described earlier [35], the periodic oscillations were associated with the vesicle formation and passage along the NT axis, evoking peristaltic transport. The TM field controlled both the onset and the time characteristics of the oscillations, effectively operating as a gating potential in field-controlled devices. We conclude that the TM field could be used to i) interrogate mechanical parameters of the NT membrane in the linear dilation regime and ii) gate the ionic and fluidic transport through the NT lumen, when coupled to the intrinsic shape instabilities of the NT system.

2. Experimental

2.1. Materials

1,2-Dioleoyl-*sn*-Glycero-3-Phosphocholine (DOPC), 1-oleoyl-2-hydroxy-*sn*-Glycero-3-Phosphocholine (OPC), 1,2-Dioleoyl-*sn*-Glycero-3-Phosphoethanolamine (DOPE), 1,2-Dioleoyl-*sn*-Glycero-3-Phospho-L-Serine (DOPS), 1-oleoyl-2-hydroxy-*sn*-Glycero-3-phospho-L-serine (OPS), fluorescently labeled 1,2-Dioleoyl-*sn*-Glycero-3-Phosphoethanolamine-N-(Lissamine Rhodamine B sulfonyl) (DOPE-Rh) and cholesterol (Chol) were from Avanti (Alabaster, AL).

We used the following lipid compositions: DOPC:Chol 7:3, DOPC:DOPE:Chol 6:1:3 and DOPC:DOPE:DOPS:Chol mixed in 4:1:2:3 M ratio to prepare parent membranes with a low bending rigidity (composition 1, bending modulus k lies in the range of 0.7–$0.9 \cdot 10^{-19}$ J); and DOPC:DOPE:OPS:Chol mixed in 3:3:2:2 M ratio to prepare parent membranes with high bending rigidity (composition 2, bending modulus k lies in the range of 3.4–$4.0 \cdot 10^{-19}$ J).

2.2. Membrane nanotubes

The nanotubes were formed using a fire-polished glass pipette (patch-clamp pipette) as described elsewhere [17,22]. For the NT production, we used two types of membrane reservoirs: planar lipid bilayer (Fig. 1A) characterized by high lateral tension (σ range 0.3–$1 \cdot 10^{-3}$ N/m, [17]) and giant supported bilayers (GSB, Fig. 1B) characterized by low lateral tension (σ range 10^{-6}–10^{-5} N/m, [22]). The tube formation was detected by fluorescence microscopy and/or conductance measurements (Fig. 1C, D, see [22] for details), while the NT length was controlled by a precise nanopositioning system [17]. The pressure was applied to the pipette interior through the micropipette holder's port using flexible Tygon tubing connected to a homemade syringe pump. Pressure monitor PM 015D (World Precision Instruments, USA) was used to control the pressure inside the pipette.

2.3. Conductance measurements

The NT conductance was measured using Axopatch 200B (Molecular Devices, Sunnyvale, CA) amplifier. The current was acquired at a voltage-clamp mode of the amplifier. The voltage applied to the pipette interior, the measured current, piezo actuator, and pressure monitor readings were digitized using the DigitData 1550 acquisition board (Molecular Devices, Sunnyvale, CA). The results were processed offline using Origin software (OriginLab, Northampton, MA). The reservoir membrane separates two compartments in the planar bilayer and the GSB systems (compartments 2 and 3, Fig. 1A, C). The GSB interior is electrically connected to the exterior media via a low-resistance (below 50MΩ) pathway associated with the contact between the membrane and the silica beads [22]. In the GSB system, the measuring electrode 1 applied the holding potential U to the pipette interior (effectively, to the NT end). The "grounding" electrode 2 kept the potential of the exterior and interior of the GSB equal to zero. In planar bilayer experiments, compartments 2 and 3 were both grounded, while the measuring electrode, as in the GSB system, controlled the pipette interior's potential.

2.4. Fluorescence microscopy

The membrane of GSB-derived NTs contained small amounts of fluorescent marker DOPE-Rh. GSB-NT was monitored using an Olympus IX-70 inverted microscope iXon+ DU885 camera (Andor Technology, Belfast, UK) with X-Cite 120 fluorescence excitation source. A 150 × 1.45-NA objective was used to ensure high-efficiency light collection at a low light level to avoid specimen photobleaching. The images were collected and processed using the ImageJ-μManager open-source software [36]. The dynamics of the fluorescence intensity were quantified using the "Z-axis profile" tool of ImageJ.
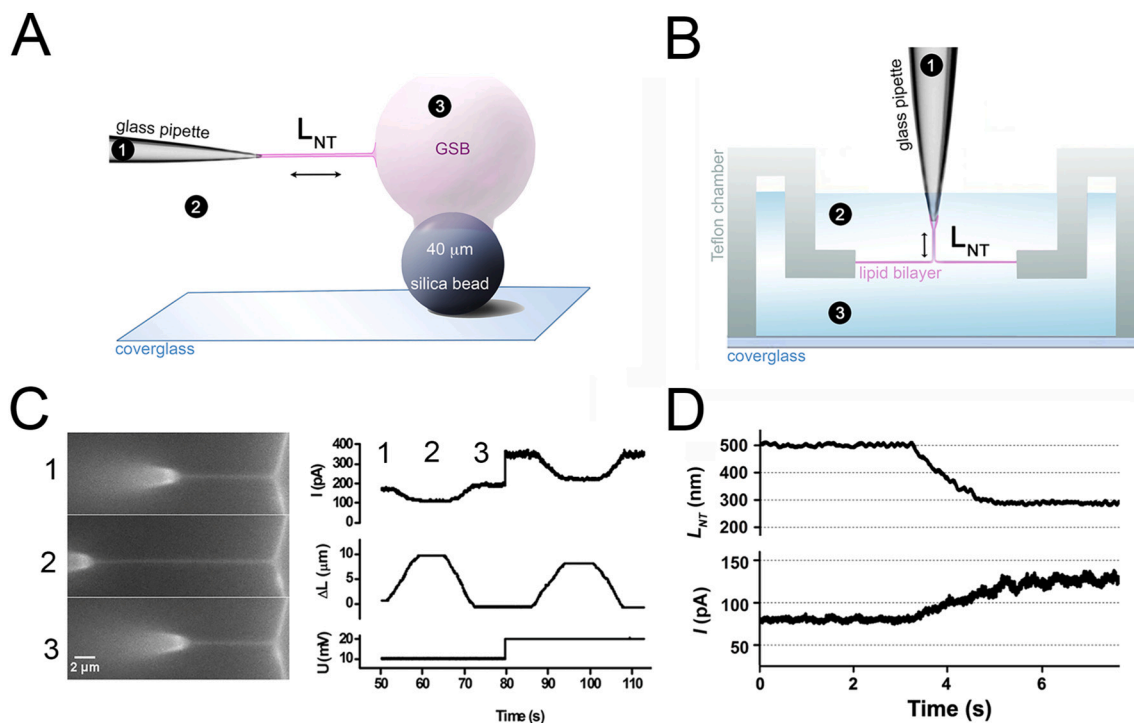
Fig. 1. Formation of lipid membrane NTs. A, B Cartoons depicting the NTs in the GSB (A) and planar lipid bilayer (B) systems. The NT connects the glass patch-pipette to the corresponding reservoir membrane. The holding potential U is applied to the electrode placed in the patch-pipette (compartment 1), the electrode also operates as a measuring electrode collecting the current through the NT lumen [17]. Compartments 2 and 3 are electrically isolated from compartment 1 and held at zero potential. In the GSB system, the GSB interior is connected to the external media via a low-resistance conductive path forming in the GSB-silica bead contact [22]. A calibrated nanoactuator is used to control the position of the patch-pipette and thus the NT length, L_{NT} [17]. B. An example of synchronized fluorescence microscopy and conductance measurements [22]. The movement of the patch-pipette produces changes in the NT length. The corresponding changes in the ionic current through the NT lumen are shown on the right. The NT conductance is obtained from the current/voltage dependence as described elsewhere [17]. D. Changes of the NT current upon submicron decrease of the NT length in the planar bilayer system.

3. Results and discussion

3.1. Ionic transport through the NT lumen is coupled to the NT dilation by the electric field

We showed earlier that the current/voltage characteristic of the NTs pulled from the planar lipid membrane reservoir (Fig. 1C, D) were nonlinear: the conductance grew proportionally to the holding potential (U) driving the ionic current through the NT lumen [17]. The conductance increase was hypothetically associated with the NT dilation by the electric field. To visualize the dilation, we used microscopic NTs pulled from GSBs labeled with a lipid fluorescent probe (Fig. 1A, B, hereafter, unless indicated otherwise, the lipid compositions with low bending rigidity (composition 1, Experimental section) were used). Simultaneous fluorescence microscopy and conductance measurements revealed that application of the incremental holding potential U caused the NT dilation increasing synchronously with the NT conductance (Fig. 2A, inset). The extent of the NT dilation depended on the amplitude
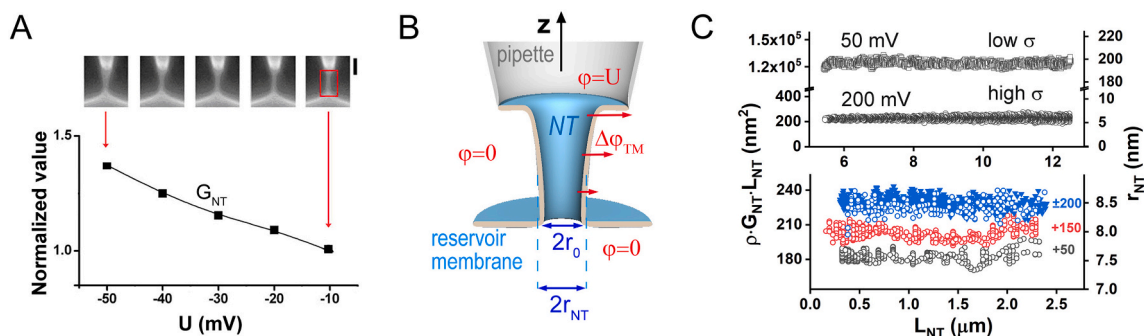

Fig. 2. Field-effect on the shape and conductance of cylindrical NT. A. Application of increasing holding potential (U) causes the NT dilation seen in the fluorescence microscopy images (above) and as the increase of the NT conductance with the voltage amplitude. Membrane fluorescence (Rh-DOPE) is shown, scale bar 2 μm. B. Schematic illustration of the NT dilation by the transmembrane voltage $\varphi(z)$ decreasing along the NT axis from the maximal value U to zero. The widening is maximal at $\varphi(z) = U$ and gradually decreases to zero at $\varphi(z) = 0$; r_c is the radius of unperturbed cylindrical NT, r_{NT} is the radius of a cylindrical NT having the same length, luminal volume, and conductance as the voltage-expanded NT. C. Upper graph: dependence of $G_{NT} \cdot L_{NT}$ (left y-axis) and r_{NT} (right y-axis) on L_{NT} measured for the NTs pulled from the GSB (low σ) and planar lipid bilayer (high σ) reservoirs. Lower graph: the dependence of $G_{NT} \cdot L_{NT}$ (left y-axis) and r_{NT} (right y-axis) on L_{NT} measured at different U (+50 mV black, +150 mV red, ±200 mV blue, with open circles and filled triangles showing the effect of positive and negative voltage respectively). (For interpretation of the references to colour in this figure legend, the reader is referred to the web version of this article.)

of the *local* transmembrane electric field, $\Delta\varphi_{TM}$ (Fig. 2B). As the NT exterior in both the GSB and the planar membrane systems was kept at zero potential (Fig. 1A, C), $\Delta\varphi_{TM}$ was maximal near the patch-pipette connection to the NT (where U is applied) and gradually decayed to zero near the reservoir membrane (Fig. 2B). The NT radius followed the same axial trend, resulting in the transformation of the NT shape from cylindrical to parabolic (Fig. 2A, B).

We next explored how this voltage-driven expansion of the NT lumen affected the parametric dependence of the NT conductance on the membrane elasticity [17]. The dependence stems from the well-known relation between the curvature and the bending rigidity of a cylindrical NT unperturbed by electric field. Its radius r_c is set by the balance of the constriction tensile force and the elastic resistance to bending [21,35]:

$$r_c = \sqrt{\frac{k}{2\sigma}} \tag{1}$$

where k is the mean curvature bending rigidity modulus and σ is the lateral tension of the reservoir membrane. The luminal ionic conductance (G_c) of such unperturbed cylindrical NT depends on its radius and length (L_{NT}) as:

$$G_c = \frac{\pi r_c^2}{\rho L_{NT}} \tag{2}$$

where ρ is the specific bulk resistance of the electrolyte in the NT lumen ($\rho = 1$ Ohm·m for 100 mM KCl at room temperature; note that for NTs containing charged lipid species, a correction has to be applied to account for counterions accumulation near the charged NT wall [17]). It follows from Eqs. (1) and (2) that $\rho G_c L_{NT}$, equal to the area of the luminal cross-section of a cylindrical NT, does not depend on the NT length. Surprisingly, we found that $G_{NT} L_{NT}$ in the voltage-expanded tubes also remained constant with L_{NT} variations (Fig. 2C, lower panel). Furthermore, $G_{NT} L_{NT}$ also scaled with σ decreasing substantially from the GSB to the planar bilayer systems (Fig. 2C, upper panel). These results indicated that $G_{NT} L_{NT}$ could be used as a length-independent parameter characterizing the dependence on the NT conductance on U. To link this parameter to the bending elasticity and tension of the NT membrane, we constructed a linear elastic model of the NT dilation.

3.2. Parametric description of small electro-elastic deformations of a membrane NT

We considered an NT connected to a reservoir membrane. A constant potential (U) was applied to the mobile NT end while that at the reservoir membrane was held at 0 potential. The NT exterior was also held at 0 potential so that U determined both the luminal and transmembrane electric fields, as shown in Fig. 2B. We assumed that the electric field produced only a small deviation from the reference cylindrical shape. The luminal radius, r_c, and the conductance, G_c, of the cylindrical NT were defined by Eqs. (1) and (2). The NT shape was parameterized by the radius $r(z)$ equal r_c at one end and gradually increasing towards the other end (Fig. 2B). In general, the electrical field effect on the NT shape has both electrostatic and dynamic (e.g. electro-osmotic) components. Here we only considered the dominating electrostatic contribution of the NT membrane capacitor, essentially, the Lippman tension [33]. The free energy density of the membrane of slightly dilated cylindrical NT can be written as:

$$F(z) = 2\pi r(z) \left(\frac{k}{2(r(z))^2} + \sigma - \frac{C_{sp}(u(z))^2}{2} \right) \tag{3}$$

where $u(z) = \Delta\varphi_{TM}(z)$ is the *local* transmembrane electric field, a function of z (Fig. 2B), and C_{sp} is the specific capacitance of the NT membrane [33,37,38]:

$$\frac{1}{C_{sp}} = \frac{1}{C_{d,1}} + \frac{1}{C_{d,2}} + \frac{1}{C_m} \tag{4}$$

where $C_{d,i}$ are the specific capacitances of the diffuse double layers and C_m is the specific capacitance of the lipid bilayer. In the electrolyte solutions used here (100 mM KCl), the Debye-Hueckel screening length (λ) is extremely small (~ 1 nm) so that

$$\frac{C_d}{2C_m} \sim \frac{\epsilon_{water}}{\epsilon_{membrane}} \frac{h}{\lambda} \sim 100 \gg 1 \tag{4´}$$

where $\epsilon_{water} \approx 80$ and $\epsilon_{membrane} \approx 2$ are the dielectric constants of water and the hydrophobic core of the lipid bilayer, respectively, and $h \sim 4$ nm is the lipid bilayer thickness. Following Eq. (4), we considered C_{sp} equal C_m, a material parameter independent of the trans-membrane field. Then the electrostatic contribution to the free energy of the NT membrane became simply proportional to U^2. We note that this dependence is specific for the NT connected to a membrane reservoir unaffected by the electric field (Fig. 1A, C). In this system, the field effect converges to recruiting additional lipid material from the reservoir, thus promoting the NT dilation. In contrast, in membrane systems of a fixed area the field effect relies on trans-membrane asymmetry and its free energy contribution depends on the asymmetry phenotype [33,39]. Yet, cellular NTs and NT networks quite generally connect large membrane compartments that could be considered reservoirs. Non-bilayer lipid storages, such as lipid droplet and proteo-lipid complexes, contribute to the reservoir capacity of the compartments and effectively control the lateral tension of the reservoir membranes [40]. Furthermore, gradients of electrochemical potentials between such compartments are also typical, seen in migratory solute and membrane transport in distributed cellular organelles [1,3,11]. Thus, Eq. (3) is not specific for a particular NT model considered here but rather covers a broader class of membrane systems with NT connections.

We next linked the field effect to the ionic transport through the NT lumen. From the Ohms law for a cylindrical conductor, we obtained the luminal ionic current I:

$$\frac{I}{2\pi r(z)} = \frac{1}{\rho} \frac{d(u(z))}{dz} \tag{5}$$

Minimizing Eq. (3) over $r(z)$ and substituting the results into Eq. (5), we derived the shape equation for $r(z)$:

$$\frac{I\rho}{\pi r_c^2} \sqrt{\frac{C_{sp}}{2\sigma}} = \frac{1}{\sqrt{(r(z)/r_c)^2 - 1}} \frac{d}{dz} \frac{r(z)}{r_c} \tag{6}$$

The solution of Eq. (6) is:

$$r(z) = r_c \cosh\left(\frac{I\rho}{\pi r_c^2} \sqrt{\frac{C_{sp}}{2\sigma}} z \right) \tag{7}$$

Integrating Eq. (7) over the NT length, we obtained the electric resistance of the field-dilated NT (R_{NT}):

$$R_{NT} = \frac{1}{I} \sqrt{\frac{2\sigma}{C_{sp}}} \tanh\left(\frac{I\rho L_{NT}}{\pi r_c^2} \sqrt{\frac{C_{sp}}{2\sigma}} \right) \tag{8}$$

Using $I = U/R_{NT} = UG_{NT}$ as a self-consistency condition, we rewrote Eq. (8) as:

$$G_{NT} = \frac{\pi r_c}{L_{NT}\rho} \frac{1}{U} \sqrt{\frac{2\sigma}{C_{sp}}} \text{artanh}\left(U\sqrt{\frac{C_{sp}}{2\sigma}} \right) = G_c \frac{\text{artanh}(\delta)}{\delta} \tag{9}$$

where $\delta^2 = \frac{C_{sp}U^2}{2\sigma}$ is a dimensionless parameter characterizing the strength of the field effect. Expanding Eq. (9) for small δ yields:

$$G_{NT} = G_c \left(1 + \frac{C_{sp}U^2}{6\sigma} \right) = \frac{\pi r_c^2}{\rho L_{NT}} \left(1 + \frac{C_{sp}U^2}{6\sigma} \right) \tag{10}$$

Eq. (10) defines the parameter $G_{NT}L_{NT}$ for the field-dilated NTs:

$$\rho G_{NT} L_{NT} = \pi r_c^2 \left(1 + \frac{C_{sp} U^2}{6\sigma}\right) = \pi r_{NT}^2 \qquad (11)$$

Consistently with experimental observations (Fig. 2C), $G_{NT}L_{NT}$ does not depend on the NT length. Moreover, as Eq. (11) exactly resembles Eq. (2), the conductance of the filed-dilated NT, like that of the reference cylindrical NT, is characterized by an effective radius r_{NT}, which does not depend on the NT length and scales with δ. In agreement with the model predictions, r_{NT} did not depend on the tube length as for the microscopic NTs obtained in GSB system as for the ultrashort NTs pulled from planar membrane reservoir (Fig. 2C). The effective radius decreased with the lateral tension (Fig. 2C, upper panel) and increased with voltage (Fig. 2C, lower panel). Importantly, the latter effect did not depend on the sign of U (Fig. 2C, blue), in agreement with Eq. (11).

As predicted by Eq. (10), the *relative* conductance increase by the electric field is linearly proportional to U^2, with the slope of linear regression inversely dependent on the system's membrane lateral tension σ (Fig. 3). In the GSB membranes with low, physiologically relevant values of the lateral tension σ [22], the NT dilation was already detected at $U = 10$ mV (Fig. 3A). Thus, small trans-membrane potentials could affect the geometry of intracellular NTs. For the NTs formed from planar lipid bilayers, application of higher U, in the range of 100 s of mV, was required (Fig. 3B), corresponding to much elevated lateral membrane tension (around 10^{-3} N/m) in this system [17]. Importantly, substituting Eq. 1 into Eq. 11 we found that r_{NT} is entirely defined by the membrane mechanics and the applied electrical potential: $r_{NT}^2 = \frac{k}{2\sigma}\left(1 + \frac{C_{sp} U^2}{6\sigma}\right)$. It follows that while the bending resistance of the NT membrane does not affect the relative NT dilation by the electric field (Eq. (10), Fig. 3), it does set the NT conductance scale (Fig. 3, inset), as well as the size cutoff for the particle transport through the NT lumen. The dependence of the NT conductance on k can be used to experimentally assess the mechanical parameters of the NT membrane [17].

So far, we have considered small alterations of the NT shape by the electric field. Their effect on the NT transport properties is minimal, as illustrated by Fig. 3. However, the situation might change near shape instability [35], where small shape perturbations could trigger a shape transformation. We next considered the field effect on the NTs nearing shape instability.

3.3. Field-effect control of the ionic transport through the shape-bistable membrane nanotube

The NT shape instabilities are mechanistically related to those of a liquid or soap film bridges extended between two coaxial endrings [35,41,42]. Within a length range defined by the endrings' size and membrane mechanics the NT has two stationary shapes, NT and catNT, with the shape transformations happening at the critical lengths (Fig. 4A, see [35] for details). One of the shape transformations occurs when the length of the cylindrical NT is decreased close to a critical value, l_c, generally below 100 nm [17,35]. Such short NTs spontaneously transform into wider catenoidal nanotubes (catNT Fig. 4A). In turn, the catNT becomes unstable at a certain critical length ($L_c > l_c$), collapsing back to the NT configuration (Fig. 4A, [35,41]). The lateral membrane tension drives the shape transformations, which, importantly, happens without rupturing the NT membrane [35]. The difference between the luminal conductance of NT and catNT can be 10–100 times (Fig. 4A), depending on the NT and the catNT diameters [35]. Here we explored how the field-driven dilation of the NT affected this dramatic shape transformation.

We applied the steps of U of progressively increasing amplitude to short, submicron NTs, held at a fixed short length close to l_c. The NT dilation was seen as the progressive increase of the G_{NT}, as well as the conductance noise, with U (Fig. 4B). Eventually, the NT dilation triggered the shape transformation, seen as an abrupt conductance increase or the NT "opening" (Fig. 4B, arrow). We next applied a constant U and slowly (0.1 μm/s) decreased the NT length until the NT opening was detected. The length at which the opening occurred increased considerably with U (for more than 10 times at $U = 200$ mV, Fig. 4C). We concluded that the transmembrane field facilitated the NT to catNT transformation by increasing the l_c, thus operating as a parametric regulator of the shape instability.

The field effect on the NT shape transformations becomes more complex when spontaneous transitions between NT and catNT occur. Such transitions, seen as oscillations of the lumen conductance between the two states corresponding to the NT and catNT conductances (Fig. 5A), were observed earlier for membranes with high bending rigidity ([35], composition 2, Experimental section). We found that the oscillations were initiated when the NT length was set inside the bistability region, either by decreasing the NT length below L_c or increasing the catNT length above l_c (Fig. 5A, red).

To understand the mechanism of these spontaneous and reversible shape transformations, we calculated the dependence on the energy barrier between the NT and catNT on the system geometry. We
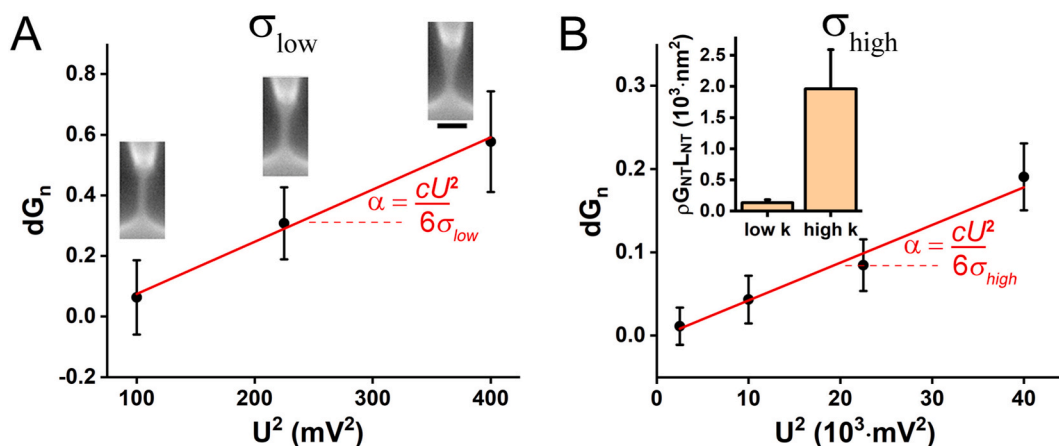

Fig. 3. Relative increase of the NT conductance $dG_n = \frac{G_{NT}(U) - G_{NT}(0)}{G_{NT}(0)}$ by the electric field bias (U) driving the ionic current through the NT lumen. A. The conductance increase in the GSB system. The fluorescence images illustrate the NT dilation by the field. Membrane fluorescence (Rh-DOPE) is shown, scale bar 2 μm. (B) The conductance increase and in the planar lipid bilayer system. The inset shows the mean values of $\rho G_c L_{NT}$ measured for the lipid membranes with low and high bending rigidity k.
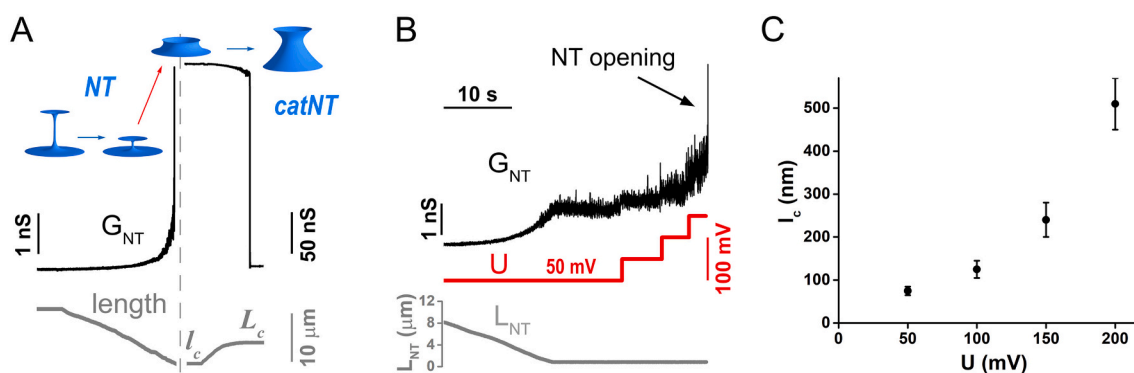
Fig. 4. The transformation of the NT to wider catNT induced by the electric field A. Decrease of the NT length towards the critical length l_c triggers spontaneous transformation (opening) of the NT to a wider catNT. The increase of the catNT length from l_c towards L_c causes the reverse transformation [35]. B. The conductance (G_{NT}, black) changes during the decrease of the NT length (L_{NT}, grey) followed by the stepwise application of progressively higher holding potential (U, red) leading to the NT opening. C. Dependence the NT length at which the opening (B) occurred on the holding potential U. (For interpretation of the references to colour in this figure legend, the reader is referred to the web version of this article.)
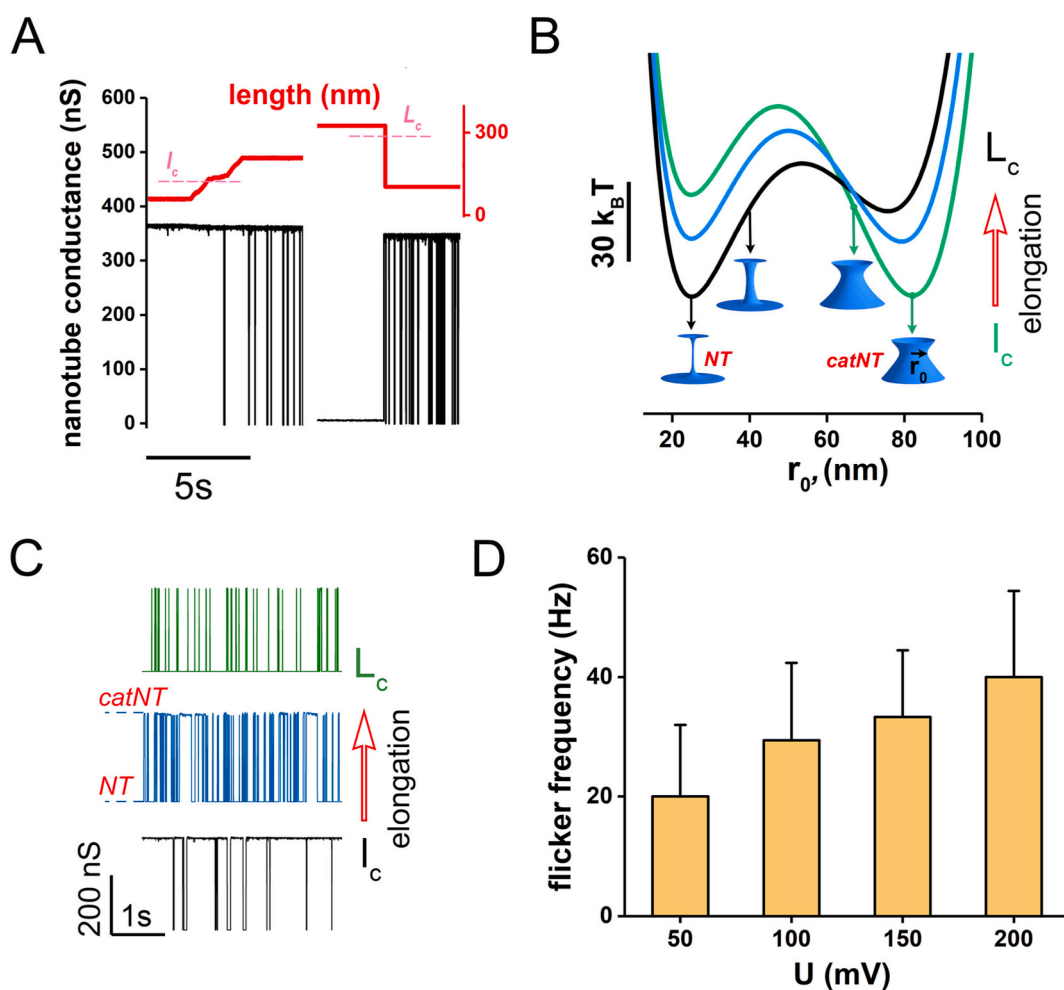

Fig. 5. Field-controlled conductance oscillations of the shape-bistable nanotube. A. Appearance of the large conductance oscillations upon driving the nanotube into the shape bistability region by either increasing the catNT length (left) or decreasing the NT length (right). B. The energy diagram illustrating the shape bistability of the nanotube [35]. The energy is parameterized by the luminal radius r_0 measured at the narrowest cross-section of the nanotube. A symmetric system was considered for simplicity, with the endrings' diameter of 240 nm and the cylindrical NT diameter of 20 nm. Two energy minima corresponding to the NT and catNT are seen. The energy branches corresponding to the variations of the NT and catNT shapes (depicted by the blue shapes) were calculated as described in the text. Black, blue and green curves illustrate energy profile alteration with the length change from sub-l_c to sub-L_c. C. Spontaneous conductance oscillations within the bistability region. Black, blue and green graphs show the conductance behavior characteristic for the free energy profiles of the corresponding colors shown in (B). D. Voltage dependence of the oscillation frequency. (For interpretation of the references to colour in this figure legend, the reader is referred to the web version of this article.)

considered the surfaces of revolution connecting to coaxial endrings of fixed radii, with unrestrictive (zero bending moment) boundary conditions at the rings [35]. We assumed that the application of the electric field produced only slight deviation from the known stationary shapes, the stable catenoid NT (catNT) and the cylindrical NT connected to the endrings by the half-catenoid "wings" ([35,43], see also the cartoons in Figs. 4A, 5B). Following earlier analyses, we also assumed that the energy barrier between these stationary shapes is defined by the energy of the unstable catenoid branch [35]. To obtain the transition trajectory from the NT to the barrier maximum, we gradually increased the radius of the cylindrical part of the NT shape while simultaneously increasing the length of the catenoidal "wings" (Fig. 5B, NT cartoon and black curve). In turn, to obtain the transition trajectory from the catNT to the barrier maximum, we expanded the catNT waist using the parabolic approximation: instead of catenary, we used parabolas to generate surfaces of revolution with progressively larger waist (Fig. 5B, catNT cartoon and green curve). The electro-elastic energy of the stationary and transitory NT shapes was calculated by integrating Eq. (3) over the area of the respective shape.

The energies of the shapes parameterized by the luminal radius in the narrowest point, r_0, are shown in Fig. 5B. Two energy minima corresponding to the stationary NT (smaller r_0) and catNT (bigger r_0), separated by a barrier, are seen (Fig. 5B). We found that the energy barrier diminishes to 20-30k_BT, enabling thermal-driven transitions [44] when the NT radius was set at ~0.1 of the endring radius (Fig. 5B), the condition satisfied in our system ($r_{NT} = 25 \pm 4$ nm for Composition 2, [32]). Furthermore, the NT and catNT minima change reciprocally with the increase of the NT length from l_c to L_c: the NT minimum becomes shallower while the catNT one grew deeper (Fig. 5B, from black to green curves). These changes of the energy diagram explained the parametric dependence of the conductance oscillations on the nanotube length obtained experimentally (Fig. 5C). In agreement with the theoretical predictions, the occurrence of the NT and catNT states changed with the increase of the NT length from l_c to L_c: catNT prevailing near l_c (Fig. 5C, black) and NT prevailing near L_c (Fig. 5C, green).

The increase of the l_c by the electric field (Fig. 4C) narrowed the bistability region thus promoting the quasi-periodic oscillation phenotype (Fig. 5C, blue curve). Accordingly, the oscillation frequency (measured as the mean interval between the sequential upward and downward conductance jumps) increased with voltage (Fig. 5D). Hence the electric field could control the onset and frequency of the conductance oscillations of shape-bistable NTs.

Of note, the holding potential amplitudes required to trigger these large-scale shape transformations of the NT produced only slight membrane deformations far from the bistability region (compare Figs. 4C and 5C). The electric field thus acted as a parametric trigger rather than a driving force. Importantly, the energy minima corresponding to the NT and catNT shapes never merge. The shape transformations are driven by thermal and mechanical noises affecting the nanotube length. The noise increase upon approaching the instability point is evident in the experiments (Fig. 4B), suggesting a possibility of stochastic resonance. The conductance oscillations could be initiated or modulated by various mechanical, electrical, or chemical processes contributing to the noise. Such triggering mechanism could be explained by seemingly random oscillations, or "flicker", of the conductance of fusion and fission pores in the cells [35,45,46].

While the stochastic oscillations of the NT conductance illustrate a highly nonlinear voltage effect, they are hardly related to the controlled nanofluidic transport. We next studied how the electric field effect controls the pressure-driven unidirectional nanofluidic transport through the NT lumen.

3.4. Voltage-dependent peristaltic transport through the NT

So far, we considered the hydrostatic pressure difference between the NT ends and across the NT wall negligible. Yet, even small pressure

gradients became notable in low-curved NTs pulled from GSB. In the GSB system, applying pressure to the pipette interior caused membrane bulging followed by a spherical droplet formation (Fig. 6A). The droplet grew until it reached the reservoir membrane and collapsed back to the NT, leading to the next transformation cycle. We related the initial membrane bulging to the pressure-driven instability of the membrane patch linking the NT to the patch-pipette rim (Fig. 6A, B). The well-known instability occurs when the pressure difference across the membrane patch (ΔP) exceeds the critical value defined as:

$$\Delta P_c = \frac{2\sigma}{R_p} \tag{12}$$

where R_p is the radius of the patch-pipette rim (Fig. 6B). Above this value, the membrane tension can no longer balance the pressure difference (neglecting the membrane bending energy contribution), and the membrane patch transforms into a growing vesicle (Fig. 6A). When the NT connecting the growing vesicle and the reservoir membrane became critically short, it opened up (Fig. 6A), as did the NTs near l_c (Fig. 4A, B above). Upon the opening, the hydrodynamic resistance of the system dropped abruptly. The fluid flux through the widely expanded nanotube lumen caused the transmembrane pressure decrease triggering the nanotube transformation back into the original cylindrical NT (Fig. 6A). Importantly, Eq. (12) indicated that if the transmembrane pressure ΔP is close to the critical value, the whole cycle of the shape transformations could be triggered by a small decrease of the local membrane tension. The link between acute tension relief and cellular membrane transformations has long been appreciated [47]. Moderate tension can develop in intracellular tubular organelles, such as the tubular endoplasmic reticulum network [48]. It is tempting to link the tension gradients to the shape instabilities propagating along the network [1,3]. Hence, we next investigated whether the periodic pressure-driven conductance oscillations seen in the microscopic GSB system could be observed in nanoscale biomimetic NTs.

The extent and kinetics of the nanotube expansion in the GSB system are seen in the synchronous changes of the integral membrane fluorescence and conductance (Fig. 6C). The pressure application ($\Delta P = 2.8 \times 10^{-2}$ atm) caused similar periodic conductance changes in the nanoscopic NTs produced from planar lipid bilayers, with the pressure release immediately aborting the oscillations (Fig. 6D). These periodic oscillations had a different triangular shape and were much slower than the stochastic oscillations seen in the shape-bistable NTs (compare Figs. 5D and 6F). Crucially, the periodic conductance oscillation could switch on and off by the electric field (Fig. 6E). Furthermore, the oscillation period depended reversibly on the holding potential amplitude (Fig. 6F), indicating a possibility of the electric field-effect control of the directed pressure-driven peristaltic transport through the NT.

To understand the mechanism of the field-effect, we created a simple thermodynamic model. We assumed that the hydrostatic pressure difference ΔP drove the vesicle growth working against the reservoir tension and heat dissipation Q. Neglecting the bending energy term, we obtain:

$$\Delta P \frac{dV}{dt} = \sigma \frac{dS}{dt} + \frac{dQ}{dt} \tag{13}$$

where V and S are the vesicle volume and area, respectively. The dissipation occured during the lipid transport from the reservoir membrane to the growing vesicle through the NT. As intermonolayer friction in the long NT is high ($\sim L_{NT}/r_{NT}$), the friction losses happened in the transition zones between the NT and the reservoir/vesicle membranes. The dissipation was approximated as $\frac{dQ}{dt} = fv^2$, where f is a surface friction coefficient, and v is the lipid flux velocity, a function of the vesicle growth speed. The growth kinetics was parameterized by the height of the vesicle cap h (Fig. 6B). Using the time parameter $a = \frac{2fR_p}{\pi r_{NT}^2 \Delta P}$ and dimensionless parameter $b = \frac{\Delta P_c}{\Delta P} < 1$ characterizing the excess P
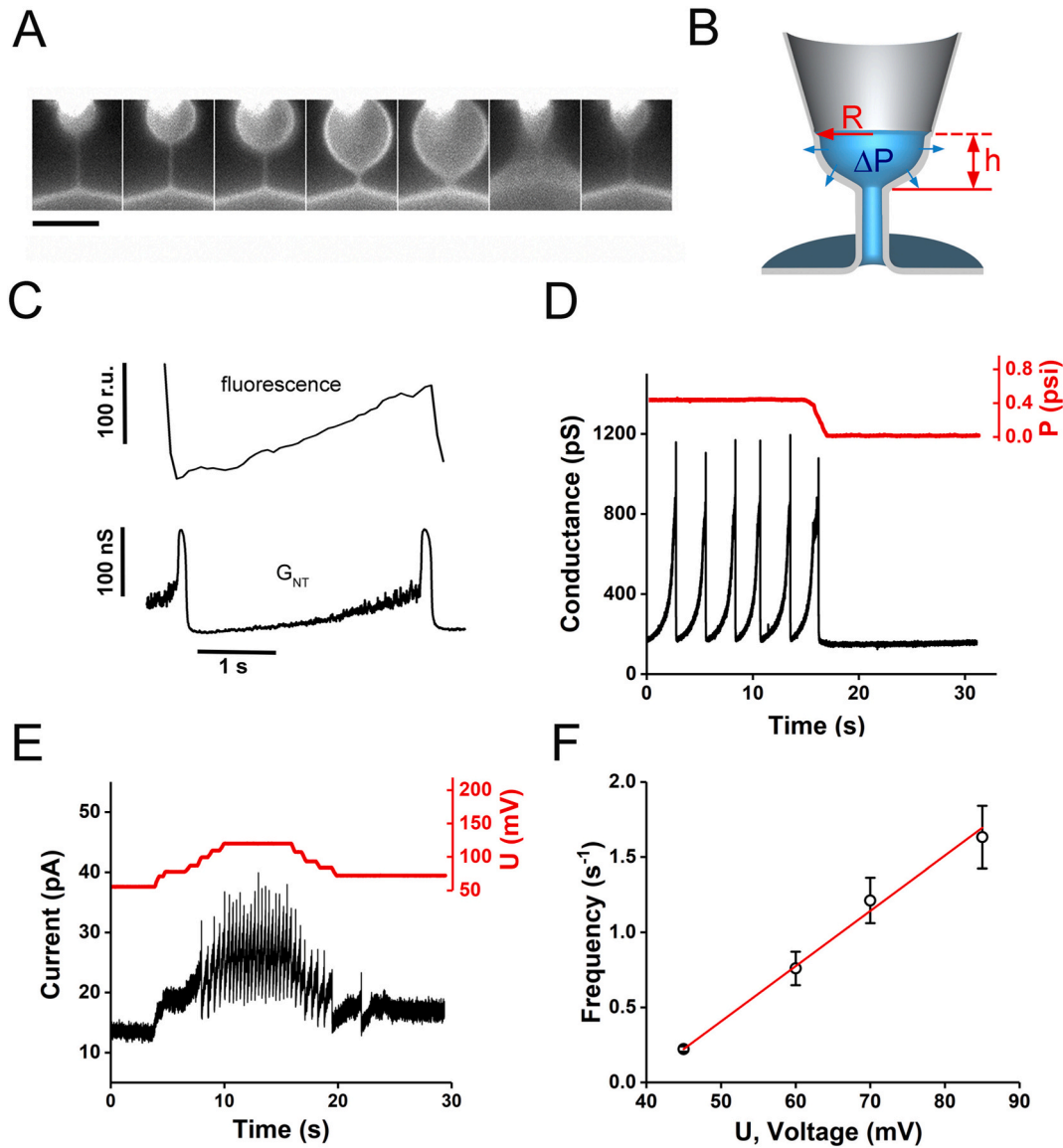
Fig. 6. Periodic oscillations of the NT shape and conductance coupled to pressure-driven transport through the NT lumen. A. Fluorescence microscopy images illustrating appearance, growth and collapse of the membrane vesicle driven by the hydrostatic pressure applied to the patch-pipette interior. Membrane fluorescence (Rh-DOPE) is shown, scale bar 10 μm. B. The cartoon illustrates the vesicle growth from the patch-pipette tip (of radius R_p) under the hydrostatic pressure (ΔP) action. The spherical segment of height h parameterizes the vesicle size. C. Changes of the ionic current through the NT lumen and total membrane fluorescence of the NT and vesicle system during the vesicle passage through the NT axis as shown in (A). D. The dependence of the NT conductance (black) on the hydrostatic pressure difference ΔP (red). The conductance oscillation seen under high ΔP disappears upon the pressure reduction. E. The electric field application affects both the appearance and the frequency of the conductance oscillations. F. The dependence of the frequency (f) of the conductance oscillations on U for short NT ($1.33L_c < L_{NT} < 2L_c$) with hydrostatic pressure approaching the critical value $\frac{2\sigma}{R}$, experimental mean values (black) and the linear fit (red, Eq. (15) with $f = 1/T$ was used) are shown. (For interpretation of the references to colour in this figure legend, the reader is referred to the web version of this article.)

driving the swelling, we obtained the growth equation:

$$\frac{1}{a}dt = \frac{h^2\,dh}{h^2 - 2bh + 1} \tag{14}$$

We further assumed that the deviation from the critical pressure is due to the tension decrease by U, equivalent to $b = \left(1 - \frac{cU^2}{2\sigma}\right)$. Considering $\frac{cU^2}{\sigma} = 1$ and integrating Eq. (14), we obtained the oscillation period (T) equal to the time required for the growing vesicle to reach the reservoir membrane (see Fig. 6A, C). We found that for the long tubes ($L_{NT} \gg R_p$) in the leading order $T = \frac{2aL_{NT}}{R_p}$. There the electric field only initiated the vesicle growth, with its kinetics independent on the field. In turn, for the short tubes ($L_c < L_{NT} < R_p$) we obtained $T = 2\pi a\sqrt{\frac{2\sigma}{cU^2}}$.

Assuming $f = 4\pi\eta$ (where η is the membrane surface viscosity) it was rewritten as:

$$T = \frac{16\pi\eta R_p^2}{k}\sqrt{\frac{2\sigma}{cU^2}} \tag{15}$$

This hyperbolic dependence fitted the experimental data well (Fig. 6F). We concluded that for the short tubes, the oscillation period, as well as the integral fluid and material fluxes through the NT lumen, could be parametrically controlled by U. The short cylindrical connections could operate as active valves in nanofluidic circuitry. Finally, we noted that the hydrostatic pressure in the output of the oscillating NTs changed periodically, suggesting another role for the oscillating NT: a peristaltic nano-pump.

We conclude by emphasizing that lipid NTs, seemingly a simple

model of intracellular tubular membrane connections, show a reach variety of nonlinear transport regimes driven and controlled by the electric field. The field effect here converges to the localized decrease of the lateral membrane tension. Such local changes of the effective tension could be associated with various intracellular membrane processes, including channel activity and action of membrane remodeling proteins [49]. Our experiments revealed that those processes could trigger dynamic transformations of the NT shape, possibly affecting not only the nanofluidic transport through the NT lumen but also other membrane processes associated with the NTs and NT networks. The electric field effect here emerges as a convenient model to study the underlying mechanisms. Further experiments will be needed to fully assess the technological and biomimetic applicability of the NTs controlled by the electric field.

Declaration of competing interest

The authors declare that they have no known competing financial interests or personal relationships that could have appeared to influence the work reported in this paper.

Author contributions

Conceptualization, V.A.F., P.V.B.; Methodology, V.A.F., P.V.B, A.V.S; Investigation, I.D.V., P.V.B., A.V.S.; Theoretical analysis, V.A.F., P.I.K., P.V.B., G.T.R.; Writing – Original Draft, V.A.F., P.V.B., A.V.S.; Writing – Review & Editing, all authors; Funding Acquisition, V.A.F., P.V.B., A.V. S.; Resources, V.A.F., P.V.B., A.V.S.; Supervision, V.A.F., P.V.B.

References

[1] S. Nehls, E.L. Snapp, N.B. Cole, K.J. Zaal, A.K. Kenworthy, T.H. Roberts, J. Ellenberg, J.F. Presley, E. Siggia, J. Lippincott-Schwartz, Dynamics and retention of misfolded proteins in native ER membranes, Nat. Cell Biol. 2 (2000) 288–295, https://doi.org/10.1038/35010558.

[2] M.J. Dayel, E.F. Hom, A.S. Verkman, Diffusion of green fluorescent protein in the aqueous-phase lumen of endoplasmic reticulum, Biophys. J. 76 (1999) 2843–2851, https://doi.org/10.1016/S0006-3495(99)77438-2.

[3] D. Holcman, P. Parutto, J.E. Chambers, M. Fantham, L.J. Young, S.J. Marciniak, C. F. Kaminski, D. Ron, E. Avezov, Single particle trajectories reveal active endoplasmic reticulum luminal flow, Nat. Cell Biol. 20 (2018) 1118–1125, https://doi.org/10.1038/s41556-018-0192-2.

[4] A.V. Shnyrova, V.A. Frolov, J. Zimmerberg, Domain-driven morphogenesis of cellular membranes, Curr. Biol. 19 (2009), https://doi.org/10.1016/j.cub.2009.07.063.

[5] C. Zurzolo, Tunneling nanotubes: reshaping connectivity, Curr. Opin. Cell Biol. 71 (2021) 139–147, https://doi.org/10.1016/j.ceb.2021.03.003.

[6] A. Rustom, R. Saffrich, I. Markovic, P. Walther, H.-H. Gerdes, Nanotubular highways for intercellular organelle transport, Science (80-.) 303 (2004) 1007–1010, https://doi.org/10.1126/science.1093133.

[7] R.E. Powers, S. Wang, T.Y. Liu, T.A. Rapoport, Reconstitution of the tubular endoplasmic reticulum network with purified components, Nature 543 (2017) 257–260, https://doi.org/10.1038/nature21387.

[8] E. Evans, H. Bowman, A. Leung, D. Needham, D. Tirrell, Biomembrane templates for nanoscale conduits and networks, Science (80-.) 273 (1996) 933 LP–935 LP, https://doi.org/10.1126/science.273.5277.933.

[9] A. Jesorka, N. Stepanyants, H. Zhang, B. Ortmen, B. Hakonen, O. Orwar, Generation of phospholipid vesicle-nanotube networks and transport of molecules therein, Nat. Protoc. 6 (2011) 791–805, https://doi.org/10.1038/nprot.2011.321.

[10] V.A. Frolov, A. Escalada, S.A. Akimov, A.V. Shnyrova, Geometry of membrane fission, Chem. Phys. Lipids 185 (2015) 129–140, https://doi.org/10.1016/J.CHEMPHYSLIP.2014.07.006.

[11] J. Espadas, D. Pendin, R. Bocanegra, A. Escalada, G. Misticoni, T. Trevisan, A. Velasco del Olmo, A. Montagna, S. Bova, B. Ibarra, P.I. Kuzmin, P.V. Bashkirov, A.V. Shnyrova, V.A. Frolov, A. Daga, Dynamic constriction and fission of endoplasmic reticulum membranes by reticulon, Nat. Commun. 10 (2019) 5327, https://doi.org/10.1038/s41467-019-13327-7.

[12] M. Simunovic, E. Evergren, I. Golushko, C. Prévost, H.-F. Renard, L. Johannes, H. T. McMahon, V. Lorman, G.A. Voth, P. Bassereau, How curvature-generating proteins build scaffolds on membrane nanotubes, Proc. Natl. Acad. Sci. U. S. A. 113 (2016) 11226–11231, https://doi.org/10.1073/pnas.1606943113.

[13] C.M. Waterman-Storer, E.D. Salmon, Endoplasmic reticulum membrane tubules are distributed by microtubules in living cells using three distinct mechanisms, Curr. Biol. 8 (1998) 798–806, https://doi.org/10.1016/s0960-9822(98)70321-5.

[14] N.B. Cole, J. Lippincott-Schwartz, Organization of organelles and membrane traffic by microtubules, Curr. Opin. Cell Biol. 7 (1995) 55–64, https://doi.org/10.1016/0955-0674(95)80045-x.

[15] A. Roux, D. Cuvelier, P. Nassoy, J. Prost, P. Bassereau, B. Goud, Role of curvature and phase transition in lipid sorting and fission of membrane tubules, EMBO J. 24 (2005) 1537–1545, https://doi.org/10.1038/sj.emboj.7600631.

[16] A. Roux, The physics of membrane tubes: soft templates for studying cellular membranes, Soft Matter 9 (2013) 6726–6736, https://doi.org/10.1039/c3sm50514f.

[17] P.V. Bashkirov, P.I. Kuzmin, K. Chekashkina, P. Arrasate, J. Vera Lillo, A. V. Shnyrova, V.A. Frolov, Reconstitution and real-time quantification of membrane remodeling by single proteins and protein complexes, Nat. Protoc. 15 (2020) 2443–2469, https://doi.org/10.1038/s41596-020-0337-1.

[18] E. Evans, A. Yeung, Hidden dynamics in rapid changes of bilayer shape, Chem. Phys. Lipids 73 (1994) 39–56, https://doi.org/10.1016/0009-3084(94)90173-2.

[19] M. Simunovic, C. Prévost, C.J. Andrew, P. Bassereau, Physical basis of some membrane shaping mechanisms, Philos. Trans. R. Soc. A Math. Phys. Eng. Sci. 374 (2016), https://doi.org/10.1098/rsta.2016.0034.

[20] T. Baumgart, B.R. Capraro, C. Zhu, S.L. Das, Thermodynamics and mechanics of membrane curvature generation and sensing by proteins and lipids, Annu. Rev. Phys. Chem. 62 (2011) 483–506, https://doi.org/10.1146/annurev.physchem.012809.103450.

[21] R.E. Waugh, R.M. Hochmuth, Mechanical equilibrium of thick, hollow, liquid membrane cylinders, Biophys. J. 52 (1987) 391–400, https://doi.org/10.1016/S0006-3495(87)83227-7.

[22] A. Velasco-Olmo, J. Ormaetxea Gisasola, J.M. Martinez Galvez, J. Vera Lillo, A. V. Shnyrova, Combining patch-clamping and fluorescence microscopy for quantitative reconstitution of cellular membrane processes with Giant Suspended Bilayers, Sci. Rep. 9 (2019), 7255, https://doi.org/10.1038/s41598-019-43561-4.

[23] J. Hurtig, B. Gustafsson, M. Tokarz, O. Orwar, Electrophoretic transport in surfactant nanotube networks wired on microfabricated substrates, Anal. Chem. 78 (2006) 5281–5288, https://doi.org/10.1021/ac060229i.

[24] M. Tokarz, B. Hakonen, P. Dommersnes, O. Orwar, B. Åkerman, Electrophoretic transport of latex particles in lipid nanotubes, Langmuir 23 (2007) 7652–7658, https://doi.org/10.1021/la700336u.

[25] C. Dekker, Solid-state nanopores, Nat. Nanotechnol. 2 (2007) 209–215, https://doi.org/10.1038/nnano.2007.27.

[26] O.M. Eggenberger, C. Ying, M. Mayer, Surface coatings for solid-state nanopores, Nanoscale 11 (2019) 19636–19657, https://doi.org/10.1039/C9NR05367K.

[27] W. Sparreboom, A. van den Berg, J.C.T. Eijkel, Principles and applications of nanofluidic transport, Nat. Nanotechnol. 4 (2009) 713–720, https://doi.org/10.1038/nnano.2009.332.

[28] A.V. Shnyrova, P.V. Bashkirov, S.A. Akimov, T.J. Pucadyil, J. Zimmerberg, S. L. Schmid, V.A. Frolov, Geometric catalysis of membrane fission driven by flexible dynamin rings, Science (80-.) 339 (2013) 1433–1436, https://doi.org/10.1126/science.1233920.

[29] L. Xue, H. Yamazaki, R. Ren, M. Wanunu, A.P. Ivanov, J.B. Edel, Solid-state nanopore sensors, Nat. Rev. Mater. 5 (2020) 931–951, https://doi.org/10.1038/s41578-020-0229-6.

[30] O.V. Krasilnikov, P.G. Merzlyak, L.N. Yuldasheva, M.F. Capistrano, Protein electrostriction: a possibility of elastic deformation of the alpha-hemolysin channel by the applied field, Eur. Biophys. J. 34 (2005) 997–1006, https://doi.org/10.1007/s00249-005-0485-9.

[31] D. Kozak, W. Anderson, R. Vogel, M. Trau, Advances in resistive pulse sensors: devices bridging the void between molecular and microscopic detection, Nano Today 6 (2011) 531–545, https://doi.org/10.1016/j.nantod.2011.08.012.

[32] P.V. Bashkirov, S.A. Akimov, A.I. Evseev, S.L. Schmid, J. Zimmerberg, V.A. Frolov, GTPase cycle of dynamin is coupled to membrane squeeze and release, leading to spontaneous fission, Cell 135 (2008) 1276–1286, https://doi.org/10.1016/j.cell.2008.11.028.

[33] P.C. Zhang, A.M. Keleshian, F. Sachs, Voltage-induced membrane movement, Nature 413 (2001) 428–432, https://doi.org/10.1038/35096578.

[34] P.V. Bashkirov, Membrane nanotubes in the electric field as a model for measurement of mechanical parameters of the lipid bilayer, Biochem. Suppl. Ser. A Membr. Cell Biol. 1 (2007) 176–184, https://doi.org/10.1134/s1990747807020110.

[35] V.A. Frolov, V.A. Lizunov, A.Y. Dunina-Barkovskaya, A.V. Samsonov, J. Zimmerberg, Shape bistability of a membrane neck: a toggle switch to control vesicle content release, Proc. Natl. Acad. Sci. U. S. A. 100 (2003) 8698–8703, https://doi.org/10.1073/pnas.1432962100.

[36] C.A. Schneider, W.S. Rasband, K.W. Eliceiri, NIH image to ImageJ: 25 years of image analysis, Nat. Methods 9 (2012) 671–675, https://doi.org/10.1038/nmeth.2089.

[37] O. Alvarez, R. Latorre, Voltage-dependent capacitance in lipid bilayers made from monolayers, Biophys. J. 21 (1978) 1–17, https://doi.org/10.1016/S0006-3495(78) 85505-2.

[38] P.V. Bashkirov, K.V. Chekashkina, A.V. Shnyrova, V.A. Frolov, Electrophysiological methods for detection of membrane leakage and hemifission by Dynamin 1, Methods Mol. Biol. 2159 (2020) 141–162, https://doi.org/10.1007/978-1-0716-0676-6_11.

[39] A.G. Petrov, Flexoelectricity of model and living membranes, Biochim. Biophys. Acta Biomembr. 1561 (2002) 1–25, https://doi.org/10.1016/S0304-4157(01) 00007-7.

[40] K. Ben M'barek, D. Ajjaji, A. Chorlay, S. Vanni, L. Forêt, A.R. Thiam, ER membrane phospholipids and surface tension control cellular lipid droplet formation, Dev. Cell 41 (2017) 591–604.e7, https://doi.org/10.1016/j.devcel.2017.05.012.

[41] S.A. Cryer, P.H. Steen, Collapse of the soap-film bridge: quasistatic description, J. Colloid Interface Sci. 154 (1992) 276–288, https://doi.org/10.1016/0021-9797 (92)90101-Q.

[42] J.B. Bostwick, P.H. Steen, Stability of constrained capillary surfaces, Annu. Rev. Fluid Mech. 47 (2015) 539–568, https://doi.org/10.1146/annurev-fluid-010814-013626.

[43] T.R. Powers, G. Huber, R.E. Goldstein, Fluid-membrane tethers: minimal surfaces and elastic boundary layers, Phys. Rev. E Stat. Nonlinear Soft Matter Phys. 65 (2002) 41901, https://doi.org/10.1103/PhysRevE.65.041901.

[44] P.I. Kuzmin, J. Zimmerberg, Y.A. Chizmadzhev, F.S. Cohen, A quantitative model for membrane fusion based on low-energy intermediates, Proc. Natl. Acad. Sci. U. S. A. 98 (2001) 7235–7240, https://doi.org/10.1073/pnas.121191898.

[45] J.M. Cabeza, J. Acosta, E. Alés, Mechanisms of granule membrane recapture following exocytosis in intact mast cells, J. Biol. Chem. 288 (2013) 20293–20305, https://doi.org/10.1074/jbc.M113.459065.

[46] W. Shin, L. Ge, G. Arpino, S.A. Villarreal, E. Hamid, H. Liu, W.-D. Zhao, P.J. Wen, H.-C. Chiang, L.-G. Wu, Visualization of membrane pore in live cells reveals a dynamic-pore theory governing fusion and endocytosis, Cell 173 (2018) 934–945. e12, https://doi.org/10.1016/j.cell.2018.02.062.

[47] A. Saric, S.A. Freeman, Endomembrane tension and trafficking, Front. Cell Dev. Biol. 8 (2021) 1736, https://doi.org/10.3389/fcell.2020.611326.

[48] A. Upadhyaya, M.P. Sheetz, Tension in tubulovesicular networks of Golgi and endoplasmic reticulum membranes, Biophys. J. 86 (2004) 2923–2928, https://doi.org/10.1016/S0006-3495(04)74343-X.

[49] M.D. El Alaoui Faris, D. Lacoste, J. Pécréaux, J.-F. Joanny, J. Prost, P. Bassereau, Membrane tension lowering induced by protein activity, Phys. Rev. Lett. 102 (2009) 38102, https://doi.org/10.1103/PhysRevLett.102.038102.